

Article

Mechano-Synthesis, Structure, and Thermal and Magnetic Behaviors of the New Compound $\text{Mn}_{1.2}\text{Co}_{0.05}\text{Fe}_{0.7}\text{P}_{0.45}\text{Si}_{0.5}\text{B}_{0.05}$

Nawel Khitouni ^{1,2}, Maha M. Almoneef ³ , Amira Mili ⁴, Mohamed Khitouni ⁵, Asma Wederni ¹ 
and Joan-Josep Suñol ^{1,*} 

¹ Department of Physics, Campus Montilivi, University of Girona, 17071 Girona, Spain; khitouninawel@yahoo.fr (N.K.); asma.wederni@udg.edu (A.W.)

² Laboratory of Inorganic Chemistry (LR 17-ES-07), Faculty of Science of Sfax, University of Sfax, B.P. 1171, Sfax 3018, Tunisia

³ Physics Department, Faculty of Science, Princess Nourah Bint Abdulrahman University, Riyadh 11564, Saudi Arabia; mmalmoneef@pnu.edu.sa

⁴ Department of Biology, Faculty of Science, Al-Baha University, P.O. Box 1988, Al-Baha 65527, Saudi Arabia; ahajsalah@bu.edu.sa

⁵ Department of Chemistry, College of Science, Qassim University, Buraidah 51452, Saudi Arabia; kh.mohamed@qu.edu.sa

* Correspondence: joanjosep.sunyol@udg.edu

Abstract: The $\text{Mn}_{1.2}\text{Co}_{0.05}\text{Fe}_{0.7}\text{P}_{0.45}\text{Si}_{0.5}\text{B}_{0.05}$ compound has been systematically synthesized by mechanical alloying for 15 h, followed by annealing with two heating cycles at 1373 K for 2 h and 1073 K for 24 h. The powder that was milled for 15 h revealed the main hexagonal- Mn_2P -type phase and the minor cubic- $\text{Mn}_3\text{Fe}_2\text{Si}$ phase through X-ray diffraction examination. After annealing the same powder at 1373 K for 2 h and again at 1073 K for 24 h, the refined phase was the unique $(\text{Mn, Fe})_2(\text{P, Si})$ type with a hexagonal structure. For the mechanically alloyed powder, the final crystallite size was approximately 20 nm, and it rose to 95 nm during the annealing process. Further, a large amount of lattice microstrain was achieved as a result of high-energy milling (about 0.75%). Over the whole temperature range of 373 to 923 K, the thermal analysis showed several overlapping exothermic peaks, which indicated the improvement of the microstructure after the structural relaxation and reordering process. Moreover, the Curie temperature of the alloy was retrieved at approximately 675 K. According to an analysis of the magnetic properties, the mechanically alloyed powder exhibited an exceptional soft ferromagnetic state after 15 h of milling, and the annealed alloy showed superparamagnetic characteristics.

Keywords: Fe_2P -type alloys; mechano-synthesis; X-ray diffraction; magnetic characteristics



Citation: Khitouni, N.; Almoneef, M.M.; Mili, A.; Khitouni, M.; Wederni, A.; Suñol, J.-J. Mechano-Synthesis, Structure, and Thermal and Magnetic Behaviors of the New Compound $\text{Mn}_{1.2}\text{Co}_{0.05}\text{Fe}_{0.7}\text{P}_{0.45}\text{Si}_{0.5}\text{B}_{0.05}$. *Inorganics* **2024**, *12*, 63. <https://doi.org/10.3390/inorganics12030063>

Academic Editor: Li Wang

Received: 19 January 2024

Revised: 15 February 2024

Accepted: 18 February 2024

Published: 20 February 2024



Copyright: © 2024 by the authors. Licensee MDPI, Basel, Switzerland. This article is an open access article distributed under the terms and conditions of the Creative Commons Attribution (CC BY) license (<https://creativecommons.org/licenses/by/4.0/>).

1. Introduction

Recent years have seen a significant increase in interest in near-room-temperature magnetic refrigeration due to its many benefits, including great efficiency and minimal environmental effects [1–3]. The effectiveness of this technique is significantly enhanced by the performance of materials with a giant magnetocaloric effect (GMCE). A first-order magnetic transformation (FOMT) frequently occurs in these advanced magnetocaloric materials [1,2,4]. Giant magnetocaloric materials having a first-order magnetoelastic transition (FOMET) have been recently referred to as the hcp- Fe_2P -type phase (space group (SG): P-26 m), and the majority of research has been conducted on $(\text{Mn, Fe})_2(\text{P, As, Ge})$ materials [1,2,5–7]. However, these materials cannot be employed in functional refrigeration systems due to the availability of Ge and the toxicity of As. Substituting As and Ge for Si is one of the most well-known strategies employed to create an ambient-temperature magnetic refrigerant with outstanding performance. Due to their GMCE performance, low economic expenses, and absence of hazardous components, $(\text{Mn, Fe})_2(\text{P, Si})$ -based

alloys have garnered significant research attention and are the most promising giant magnetocaloric materials (GMCs) when compared to the previous two-generation (Mn, Fe)₂(P, As) and (Mn, Fe)₂(P, Ge)-based composites [8,9]. MnMX alloys (where M = Co or Ni and X = Si or Ge) have typically been the focus of extensive investigation because of the reliance on magnetic and structural degree behaviors [10–12]. During the cooling process, the structural transition of stoichiometric MnMX compounds occurs from a martensitic-like hexagonal Ni₂In structure to an orthorhombic TiNiSi structure [13]. The primary issue with MnMX compounds is that the transformation between two paramagnetic states occurs at a temperature that is typically much higher than the magnetic-ordering temperatures of both the hexagonal (paramagnetic) and orthorhombic (ferromagnetic) phases. This leads to low magnetization and a low magnetic-field-driving capacity [13,14]. A significant amount of GMCs is produced by the magnetic-field-induced magneto-structural transformation (MST) from the hexagonal to the orthorhombic phases because of the large magnetization difference between the two phases [14]. Potential applications utilizing magneto-responsive effects require an MnMX compound type with MST that has a large Curie temperature domain and low magnetization. MnNiSi, an example of the MnMX family, possesses a considerably large Curie temperature domain with a high Curie temperature (T_C) of 622 K [15]. Furthermore, from the perspective of application, the (Mn, Fe)₂(P, Si)-based materials must have a continuously variable temperature change (T_C) close to the working temperature and very small thermal hysteresis, which must be at least smaller than their adiabatic temperature change. Since the (Mn, Fe)₂(P, Si) system was discovered, numerous attempts have been made to achieve high T_C and small thermal hysteresis while maintaining the GMCE. These attempts have included changing the Mn/Fe and/or P/Si ratio [16], substituting Mn and Fe with other transition metals and rare earths [17], and replacing P or Si with B [9,18]. Without sacrificing the GMCE, it has been discovered that boron substitution improves the mechanical stability and significantly reduces the thermal hysteresis [18,19].

Since MnMX undergoes an orthorhombic–hexagonal structural change as the temperature range changes, accompanied by a magnetic transition from a ferro- to a paramagnetic state, we have chosen it as the starting material, where M = Co and Fe and X = P and Si. To the best of our knowledge, the structural and magnetic properties of the mechanically alloyed (MA) MnCoFePSiB have not yet been evaluated in detail, nor has the phase evolution been fully analyzed. Until now, work on adding minor metalloids to magnetocaloric alloys as good modified elements has been limited. Additionally, there are numerous options to optimize the milling parameters, including the time, speed, and ball-to-powder ratio, to increase the energy efficiency of mechanical milling for the production of magnetocaloric alloys. The current work focuses on both the synthesis of the Mn_{1.2}Co_{0.05}Fe_{0.7}P_{0.45}Si_{0.5}B_{0.05} alloy using the ball milling technique and the characterization of the phase transformation throughout the annealing process and its effects on the magnetic characteristics.

2. Results and Discussion

2.1. SEM Analysis

Figure 1 presents the scanning electron microscopy (SEM) images (in the electron backscatter mode) and the corresponding energy-dispersive X-ray spectrometry (EDS) analysis of the MA-Mn_{1.2}Co_{0.05}Fe_{0.7}P_{0.45}Si_{0.5}B_{0.05} powder mixtures obtained after 15 h of milling. The majority of the mixing powder particles have irregular morphologies, whereas a minority have spherical morphologies. This is because of the competing impacts of fracture, cold welding, and plastic deformation. The small particles are cold-welded on the large particles' surfaces, which may promote the growth of some particles relative to the smallest ones. The powder particles' sizes appear to be dispersed throughout a large range (0.8–5 μm). However, Si particles are more brittle and harder than Mn, Fe, and Co particles. As a result, they fracture, and the smaller particles agglomerate together to produce lamellar particles, which in turn form agglomerated particles of various sizes and forms. In addition, extreme plastic deformation makes the metallic particles brittle and increases their propensity to bond to form larger particles. The macrostructure, which is

divided into two phases—the lightest (object 1) and darkest (object 2) areas—appears more distinct at high magnification. The darker portions correspond to the primary hexagonal phase of the Mn_2P type, while the lighter areas reflect the alpha-Mn-rich phase indicated by the impurity $\text{Mn}_3\text{Fe}_2\text{Si}_3$ (found by X-ray diffraction (XRD)). The depiction is shown without the peaks corresponding to the Co and B elements because the EDS resolution was insufficient to detect such low content of Co and B (0.05 at%).

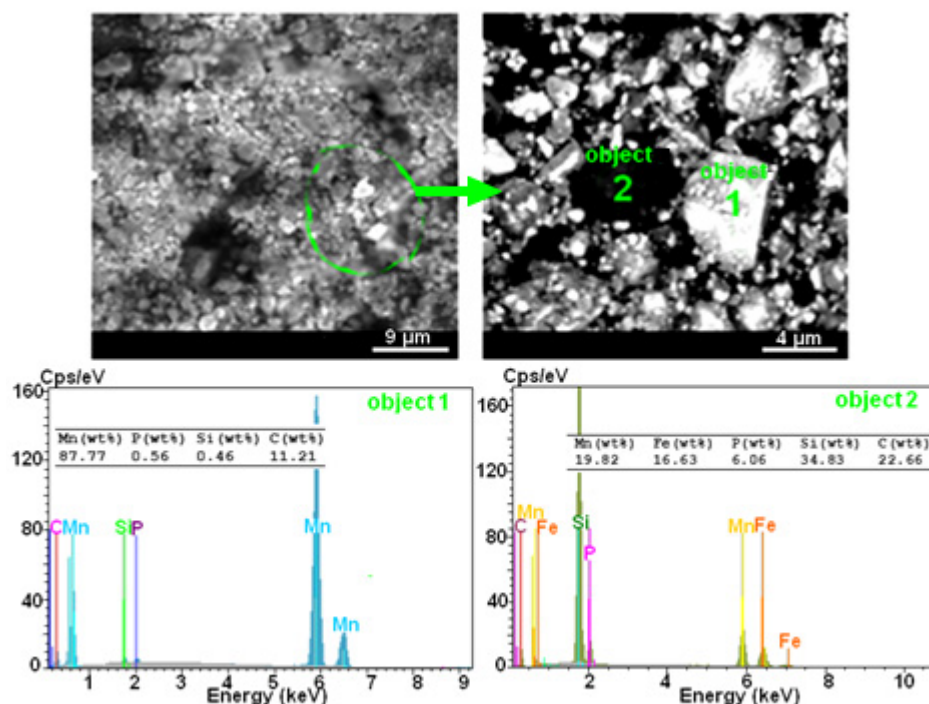


Figure 1. SEM images (in the electron backscatter mode) of the $\text{Mn}_{1.2}\text{Co}_{0.05}\text{Fe}_{0.7}\text{P}_{0.45}\text{Si}_{0.5}\text{B}_{0.05}$ powder mixtures milled for 15 h and the corresponding EDS analysis.

Figure 2 illustrates the SEM image and the corresponding EDS analysis of the MA- $\text{Mn}_{1.2}\text{Co}_{0.05}\text{Fe}_{0.7}\text{P}_{0.45}\text{Si}_{0.5}\text{B}_{0.05}$ powder mixtures obtained after 15 h of milling, followed by annealing with two heating cycles (at 1373 K for 2 h and again at 1073 K for 24 h). The SEM image reveals that the microstructure is composed of granules of round and elongated shapes with lenticular interfaces. This microstructure is explained by its adaptation to the large strain energy induced by the significant lattice distortions between the paramagnetic and ferromagnetic phases [20].

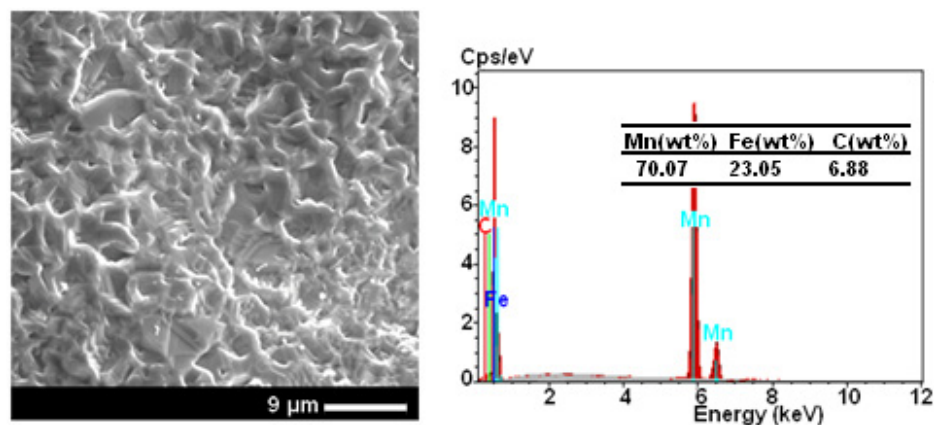


Figure 2. SEM image (in the electron backscatter mode) of the $\text{Mn}_{1.2}\text{Co}_{0.05}\text{Fe}_{0.7}\text{P}_{0.45}\text{Si}_{0.5}\text{B}_{0.05}$ powder mixtures obtained after 15 h of milling, followed by annealing with two heating cycles, and the corresponding EDX analysis.

2.2. XRD Analysis

Figure 3 presents the XRD patterns of the $\text{Mn}_{1.2}\text{Co}_{0.05}\text{Fe}_{0.7}\text{P}_{0.45}\text{Si}_{0.5}\text{B}_{0.05}$ powder mixtures obtained after 15 h of milling and after annealing with two heating cycles (two heating cycles at 1373 K for 2 h and then at 1073 K for 24 h, separated from each other by quenching in water). Structure determination and refinement of the XRD pattern of the MA sample indicates the coexistence of the cubic $\text{Mn}_3\text{Fe}_2\text{Si}$ (CIF: 1539791 [21]; SG: Fm-3m; $a = 0.8935$ (1) nm) minor phase with a weight fraction of 17.1(3) wt.% and a hexagonal Mn_2P type (CIF: 1539073 [22]; SG: P-62m; $a = 0.5875$ (1) nm and $c = 0.3642$ (2) nm) as the main phase (82.9 (3) wt.%). The presence of the hexagonal Mn_2P structure type may be justified by the value of the ratio Mn/Fe and the initial quantity of powder, such that the Mn reacts with the P atoms [23]. After annealing with two heating cycles, one can remark that the peaks relating to the cubic phase of the $\text{Mn}_3\text{Fe}_2\text{Si}$ type almost disappear and only the reflection patterns of the Mn_2P -type structure (SG: P-62m; $a = 0.6071$ (1) nm and $c = 0.3461$ (2) nm) are observed. According to the present results, the cubic $\text{Mn}_3\text{Fe}_2\text{Si}$ impurity can be removed after 2 h of annealing at a high temperature of 1373 K.

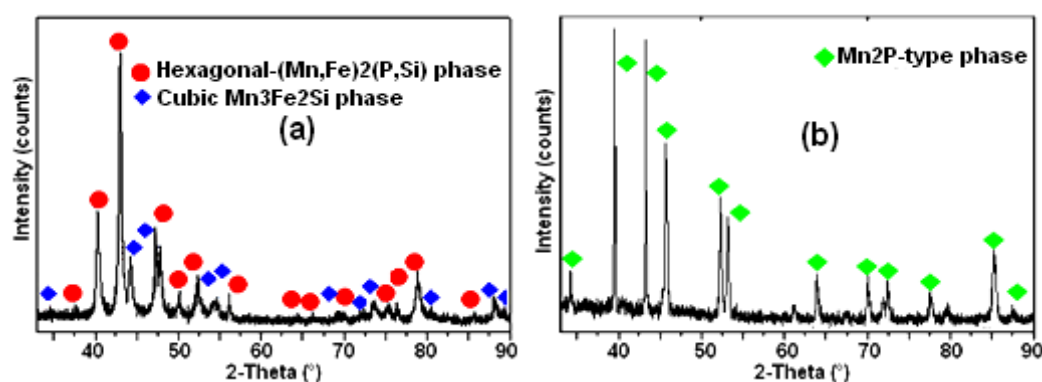


Figure 3. XRD patterns of $\text{Mn}_{1.2}\text{Co}_{0.05}\text{Fe}_{0.7}\text{P}_{0.45}\text{Si}_{0.5}\text{B}_{0.05}$ powders: (a) after 15 h milling and (b) after annealing with two heating cycles (at 1373 K for 2 h and then at 1073 K for 24 h).

Figure 4 shows the Rietveld refinement of the XRD patterns for the two synthesized powders: that of the powder milled for 15 h and that of the same powder ground and then annealed according to the two treatments with two heating cycles (at 1373 K for 2 h and then at 1073 K for 24 h). The Rietveld refinement reveals, for the MA powder, the formation of alpha Mn-type and hexagonal Mn_2P -type phases. After annealing the same powder at 1373 K for 2 h and then at 1073 K for 24 h, the refined phase is the unique $(\text{Mn}, \text{Fe})_2(\text{P}, \text{Si})$ type with a hexagonal structure. This structure has been described by Miao et al. [24] and is given in the inset of Figure 4b. The Mn atoms (red) preferentially occupy the pyramidal coordinated 3g sites with five nonmetals as the nearest neighbors, while the Fe atoms (blue) favor the tetragonal coordinated 3f sites surrounded by four nonmetal coordination atoms and the P/Si atoms are randomly distributed on the 2c and 1b sites.

As a consequence of the mechano-synthesis technique for 15 h, the diffraction peaks are quite broad, indicating the nanocrystallization of the processed powder mixture.

The Rietveld refinement of the average crystallite sizes for the MA powder mixtures was found to be approximately 15 and 25 nm (Table 1), for the alpha Mn and the hexagonal Fe_2P -type phases, respectively. The size of a crystallite, which is not always the same as the particle size seen by the use of SEM investigation, is thought to be the size of a coherently diffracting domain. Moreover, the same phases are expected to have lattice strain values of approximately 0.87 (alpha Mn) and 0.65% (hexagonal Mn_2P) (Table 1). The lattice contraction or expansion in the crystallites, which is the source of the lattice microstrain, is mostly caused by the arrangement of atoms within the crystal lattice. On the other hand, many structural defects (point defects like vacancies, stacking faults, grain boundaries, etc.) are also created in the lattice structure as a result of size refinement and internal–external stresses that result in lattice strain [25,26]. For the annealed sample, the

estimated crystallite size and lattice strain values were found to be approximately 95 nm and 0.085% (Table 1), respectively. Berrak and Heumann [27] showed that this hcp Mn_2P -type structure is the most stable at a higher temperature for a system with a large amount of Mn. Moreover, Lai et al. [28] have shown the same results during the synthesis of a Mn-Fe-P-Si-B system by arc melting. It can be noted that an increase in the lattice parameter, a , of $\Delta a = 0.0196$ nm, associated with a decrease in the lattice parameter (c) of $\Delta c = -0.0182$ nm, allows a decrease in the ratio c/a value from 0.62 to 0.57. In addition, the size of the crystallites of the hcp Mn_2P -type phase increased by $\Delta D = 70$ nm after annealing; this increase may be along the (a) axis of the lattice. This relaxation in the microstructure may be related to the decrease in the dislocation's density effect. Guillou et al. [18], in their study of the structural, magnetic, and calorimetric evolutions of $MnFe_{0.95}P_{0.67-x}Si_{0.33}B_x$ samples during heating, reported that the discontinuous nature of the ferromagnetic transition may be caused by the combined effect of the quenching of the $3f$ moments (pyramidal coordinated sites preferentially occupied by Fe atoms) and the loss of long-range order on the $3g$ sites (tetragonal coordinated sites preferentially occupied by Mn atoms). It is believed that this $3f$ quenching would result from a modification in the electronic structure, which is accompanied by a strong magnetoelastic effect: when heated, the basal plane (a and b axes) contracts, and the c axis expands, raising the c/a ratio. In addition, it was previously reported [19] that the c -axis lattice parameter increases with temperature, while the a and b axes (basal plane) exhibit negative thermal expansion. The same authors used a strain gauge dilatometer to measure the linear thermal expansion ($\Delta l/l$) of a single crystal of Fe_2P upon cooling through the first-order-type magnetic transition and found a sharp increase of $\Delta a/a = 0.74 \times 10^{-3}$ with a simultaneous decrease in the c axis ($\Delta c/c = -0.84 \times 10^{-3}$).

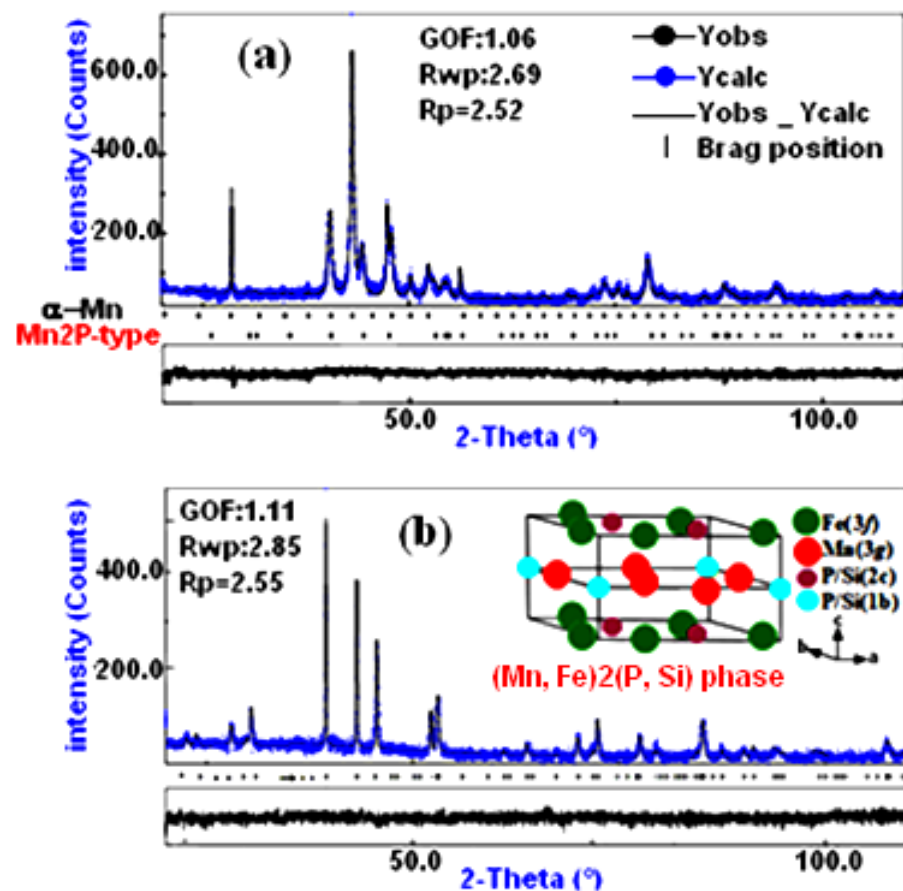


Figure 4. Rietveld refinements of XRD patterns of MA $Mn_{1.2}Co_{0.05}Fe_{0.7}P_{0.45}Si_{0.5}B_{0.05}$ powders for 15 h (a) and annealing with two heating cycles (at 1373 K for 2 h and then at 1073 K for 24 h) (b). Inset of (b): Schematic representation of $(Mn, Fe)_2(P, Si)$ lattice [20].

Table 1. Lattice parameters (a, b, and c), proportion of phases (%), crystallite size <D>, and lattice microstrain < ϵ > of the MA $\text{Mn}_{1.2}\text{Co}_{0.05}\text{Fe}_{0.7}\text{P}_{0.45}\text{Si}_{0.5}\text{B}_{0.05}$ powders obtained after 15 h milling and after annealing with two heating cycles.

Powder	Phase Type	a (nm)	c (nm)	c/a	Phase (%)	D (nm)	ϵ (%)
Milled powder	$\alpha\text{-Mn}_3\text{Fe}_2\text{Si}$	0.8935 (1)	-	-	17.1	15	0.870
	hcp- Mn_2P	0.5875 (1)	0.3642 (1)	0.61	82.9	25	0.650
Annealed powder	hcp-(Mn,Fe) $_2$ (P,Si)	0.6071 (1)	0.3460 (1)	0.56	100.0	95	0.085

2.3. Thermal Analysis

Figure 5 shows the differential scanning calorimetry (DSC) curve of the MA $\text{Mn}_{1.2}\text{Co}_{0.05}\text{Fe}_{0.7}\text{P}_{0.45}\text{Si}_{0.5}\text{B}_{0.05}$ powders obtained after 15 h of milling and after annealing with two heating cycles. For the milled sample, several overlapping exothermic peaks, spread over the whole temperature range from 373 to 923 K, are revealed. The first exothermic peak at 536 K (labeled (1)) can be related to FOMT [23]. The corresponding heat release was calculated to be around 11 J/g. An endothermic peak (labeled (2)) occurs in the temperature range of 648–698 K, which can be ascribed to the Curie temperature of the $\text{Mn}_{1.2}\text{Co}_{0.05}\text{Fe}_{0.7}\text{P}_{0.45}\text{Si}_{0.5}\text{B}_{0.05}$ powder. The extracted Curie temperature is around 675 K. It should be noted that this T_c value is higher than that measured for Mn_2RuxGa (625 K) [29] and lower than that measured for $\text{Mn}_2\text{Fe}_{0.73}\text{Ga}$ (695 K) [30] thin films. The highest value of T_C was also found by Levin et al. [31] for MnCoP alloy (578 K). Indeed, the doping of the alloy by boron leads to a strong increase in T_C [9,18]. This peak is followed by a shoulder (labeled (3)) that spreads out in the temperature range of 698–773 K. It can be linked to the disappearance of the important volume fraction of structural defects, mainly dislocation defects. The high-intensity peak at 843 K (labeled (4)) might be due to long-range ordering. The recovery in terms of dislocation annihilation and reordering are related processes that may occur simultaneously. The peak noted (5) may be due to the beginning of obtaining the pure hexagonal phase of the Mn_2P type after the disappearance of the cubic impurity $\text{Mn}_3\text{Fe}_2\text{Si}$. In the same context, Singh et al. [32] studied, by XRD analysis, the effect of heat treatment on the phase purity of Fe_2P powder synthesized by ball milling. They noticed the complete disappearance of the tetragonal Fe_3P -type phase impurity after annealing at 1123 K/24 h and they consequently obtained a unique hexagonal-type Fe_2P phase.

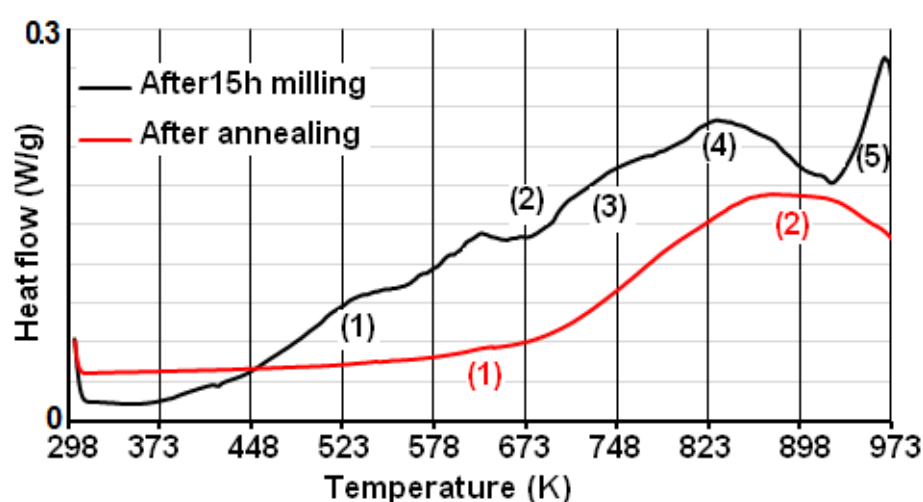


Figure 5. DSC curve of the $\text{Mn}_{1.2}\text{Co}_{0.05}\text{Fe}_{0.7}\text{P}_{0.45}\text{Si}_{0.5}\text{B}_{0.05}$ powder obtained after 15 h of milling and after annealing with two heating cycles.

In the case of the annealed sample, we notice two peaks: the first one occurs at the temperature of 663 K, which can be ascribed to the T_c of the pure Mn_2P -type phase obtained after two heating cycles. Compared with the MA sample for 15 h, the annealed one with

two heating cycles at 1373 K/2 h and then 1073 K/24 h shows a 285 K decrease in T_C heating. It is possible to identify extrinsic (such as the dynamic sweeping rate) and intrinsic (such as the electrical properties) contributions to the cause of this decrease in the T_C value [33]. The second peak (labeled (2)) may be due to the good crystallized system with large grains, devoid of structural defects such as dislocations.

2.4. Magnetic Analysis

Figure 6 presents the magnetic hysteresis curves, measured at room temperature, of the $Mn_{1.2}Co_{0.05}Fe_{0.7}P_{0.45}Si_{0.5}B_{0.05}$ powders obtained after 15 h milling and after annealing with two heating cycles at 1373 K for 2 h and then at 1073 K for 24 h. A sigmoidal form with little loss is revealed by the hysteresis loop in the case of the milled powder, demonstrating ferromagnetic activity and the behavior of nanostructured materials with tiny magnetic domains [33]. With the support of nanocrystalline ferromagnetic materials, a variety of phenomena, including soft (magnetic coercivity (H_c) < 12.56 Oe), hard (H_c > 12.56 Oe) [34], and superparamagnetic ($H_c \sim 0$ Oe) [35] behaviors, have been advantageously produced. According to the current investigation, the mechanically alloyed $Mn_{1.2}Co_{0.05}Fe_{0.7}P_{0.45}Si_{0.5}B_{0.05}$ alloy has an excellent soft ferromagnetic feature after 15 h, as indicated by the calculated H_c value of 7.36 Oe. The requirement for extremely low hysteresis losses was stated by Nowroozi et al. [36] for soft magnetic materials. According to our research, this H_c value is lower than those found in other published studies, which include 45 Oe for CoCrFeNiCuAl high-entropy alloy (HEA) [37], 175.68 Oe for CoCrFeNiMn HEA [38], and 30.23 Oe for $(Al_{19}Co_{20}Fe_{20}Ni_{41})_{100-x}B_x$ HEA [36]. In addition, the estimated values for the saturated magnetization (M_s) and remanence ratio (M_r/M_s) are as follows: 2.65% (1.27 for $(Al_{19}Co_{20}Fe_{20}Ni_{41})_{100-x}B_x$ HEA [39], 2.95 for CoCrFeNiMn HEA [40], and 5.98% for CoCrFeNiCuAl HEA [38]) and 7.36 Oe (30.23 for $(Al_{19}Co_{20}Fe_{20}Ni_{41})_{100-x}B_x$ HEA [39], 175.68 Oe for CoCrFeNiMn HEA [40], and 45 Oe for CoCrFeNiCuAl HEA [38]), respectively. Further research on the magnetic characteristics of CoCrCuFeNiTi $_x$ alloys by Zhang et al. [41] revealed saturation magnetization lower than 2 emu/g. When compared to the magnetic properties of HEAs found in the existing literature [38–40], the current MnCoFePSiB HEA has similar values for low H_c , M_s , and M_r/M_s . Notably, good soft magnetic performance was achieved with high M_s and low H_c values. The current outcome shows that the as-milled powder has an excellent soft magnetic characteristic and can be used as a soft magnetic material. The investigation by Feng et al. [39] indicates that element B is beneficial to the use of alloys as soft magnetic materials.

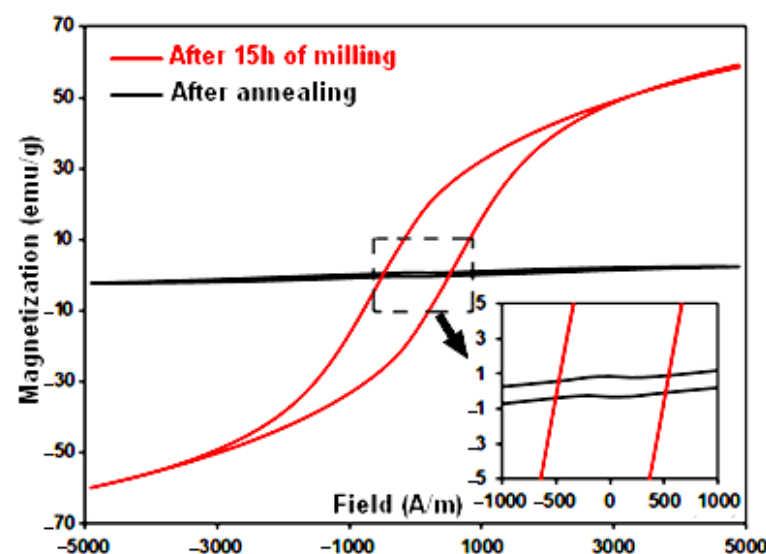


Figure 6. Magnetic hysteresis curves, measured at room temperature, of the $Mn_{1.2}Co_{0.05}Fe_{0.7}P_{0.45}Si_{0.5}B_{0.05}$ powders obtained after 15 h milling and after annealing with two heating cycles (at 1373 K for 2 h and then at 1073 K for 24 h). The inset corresponds to the (0,0) region.

Under a magnetic field of 20,000 Oe, the as-annealed MnCoFePSiB powder's magnetic hysteresis curve has a superparamagnetic characteristic, with M_s of 0.025 emu/g, M_r/M_s of 3.048%, and H_c of 17.35 Oe. The result of the phase change and structure coarsening is this unique phenomenon of magnetic development during annealing [41]. The displayed grain size of the annealed HEA is around 85 nm, as previously demonstrated, which is large enough to cause superparamagnetic behavior. It is commonly known that magnetic nanoparticles smaller than 100 nm may exhibit superparamagnetic properties [38,41–43]. Additionally, the magnetic characteristics of the $Ti_xCoCrCuFeNi$ and $(Al_{19}Co_{20}Fe_{20}Ni_{41})_{100-x}B_x$ HEAs were studied by Zhang et al. [41] and Feng et al. [39]. They found that, respectively, the magnetic properties of these alloys changed as the Ti and B content increased. Nevertheless, there is no shift in the metal element ratios in the current alloy system. Thus, the outcome is irradiative, suitable for additional use under particular conditions.

As a result, a shift in structure is correlated with a shift in magnetic behavior; that is, before reaching a superparamagnetic regime, there may be a transition from ferromagnetic to paramagnetic behavior. As previously demonstrated [44], the Fe_2P -type phase exhibits a notable change in the c/a ratio of the hexagonal structure, along with a first-order magnetic transition (FOMT) from a ferromagnetic (FM) state to a paramagnetic one (PM), with lattice distortion caused by the magnetoelastic effect. Furthermore, it is shown that for temperatures considerably above T_C , the paramagnetic susceptibility differs from the Curie–Weiss law. However, because a magnetoelastic-like transition accompanies the field-induced PM-FM transition, the latter typically identifies substances displaying a first-order transition. The system's dynamic properties, such as the lattice entropy, could be altered by this behavior. Conversely, the production of a nanostructure and/or amorphous phases may be linked to the superparamagnetic phase. As mentioned earlier, the powder's as-milled size is about 10 nm, which is small enough to cause superparamagnetic behavior. It is commonly known that magnetic nanoparticles smaller than 10 nm exhibit superparamagnetic behavior [43,45]. Using exchange coupling analysis based on DFT calculation, Liu et al. recently connected the crucial Fe-Fe distances to the metamagnetic transition of the Fe moment at the 3f site [46].

3. Materials and Methods

The $Mn_{1.2}Co_{0.05}Fe_{0.7}P_{0.45}Si_{0.5}B_{0.05}$ alloy was prepared from elemental powders Mn (purity~99.3%), Co (purity~99.5%), Fe (purity~99.5%), P (purity~98.9%), Si (purity~99.99%), B (purity~98%), and Fe_2P (purity~99.5%). Mechanical alloying using a Fritsch P7 ball mill (BM) in an argon atmosphere for 15 h at 450 rpm was performed to achieve the synthesis. Afterward, the milled powder was enclosed in quartz bulbs under an argon atmosphere. Finally, this powder was annealed with two heating cycles at 1373 K for 2 h and then at 1073 K for 24 h, separated from each other by quenching in water.

By the use of SEM (Type DSM960A ZEISS, Carl Zeiss GmbH, Oberkochen, Germany) in secondary electron mode at a voltage of 15 kV, the morphology of the particle powders was examined. The EDS analyzer Vega©Tecan was mounted in the SEM. The size distribution of the particles was obtained from the SEM images by ImageJ software analysis (Version 1.51j8, National Institutes of Health, Bethesda, MD, USA)). The erode and despeckle algorithms were applied to isolate the particle images from the background, and the remaining touching particles were removed manually prior to the calculation of the size distribution.

The milled powders were examined by the XRD method, using a Siemens D500 powder diffractometer in $(\theta-2\theta)$ geometry using $CuK\alpha$ radiation ($\lambda_{Cu} = 0.15418$ nm). The phase analysis was performed by using the International Center for Diffraction Data (ICDD) (PDF-2, 2012) files. Both structural and microstructural parameters were determined from the refinement XRD patterns using the MAUD program (version 2.55) based on the Rietveld method [47].

A thorough analysis of the XRD profiles can be carried out in the framework of the MAUD software [47] using Rietveld refinement and the Warren–Averbach (W-B) method [48,49]. This enables the determination of the phase composition as well as structural and microstructural parameters for each phase, including the lattice parameters, average crystallite size $\langle D \rangle$, and lattice microstrain (ϵ). It is feasible to compute a statistical parameter, known as the goodness of fit “ χ^2 ”, which is the ratio of the standard agreement indices, R_{wp} to R_{exp} , and must increase towards unity for a successful refinement:

$$\chi^2 = \frac{R_{wp}}{R_{exp}} \quad (1)$$

The profile refinements continue until convergence is reached; the value of the quality factor “ χ^2 ” (the goodness of fit index (GOF)) is approaching 1.

As shown previously, the average crystallite size, $\langle D \rangle$, and lattice distortions, (ϵ), yield line broadening. Thus, the total line broadening β of the diffraction peak can be expressed using the Williamson–Hall (WH) approach as [50]

$$\beta = \frac{k\lambda}{D} \frac{1}{\cos\theta} + 4\epsilon \tan\theta \quad (2)$$

where k is the shape factor, λ is the X-ray wavelength, θ is the Bragg angle of a reflection (hkl), D is the crystallite size, considered as the size of a coherently diffracting domain, and ϵ is the lattice strain (uniform lattice microstrain) caused by crystal flaws in the nanocrystals along the crystallographic direction. The first term in the right-hand part of Equation (2) is the size contribution and the second term is the lattice distortion. If the peak broadening is due solely to a finite crystallite size, it is assumed that $\beta = k\lambda/(\langle D \rangle \cos\theta)$, where the shape factor has a typical value of about 0.9, but varies with the actual shape of the crystallite; this is known as the Scherrer equation.

The DSC measurements were carried out using a Mettler-Toledo DSC822 type calorimeter in the temperature range of 298 to 923 K and with a speed range of 10 K/min.

The superconducting quantum interference equipment of Quantum Design (Caledonia, MI, USA) SQUID MPMS-XL was employed to measure the M_s , M_r , and H_c of the as-alloyed powders at 300 K, with a maximum applied field of 50 kOe.

4. Conclusions

In this paper, we report on the mechano-synthesis and structural, thermal, and magnetic characterization of the nominal $\text{Mn}_{1.2}\text{Co}_{0.05}\text{Fe}_{0.7}\text{P}_{0.45}\text{Si}_{0.5}\text{B}_{0.05}$ alloy. The XRD result confirmed that the nanocrystalline cubic $\alpha\text{-Mn}_3\text{Fe}_2\text{Si}$ and the hcp- Mn_2P -type structure occurred upon milling for 15 h. Meanwhile, after two heating cycles and annealing, an hcp- Mn_2P -type structure becomes the main phase. The refined crystallite size value is around 15–25 nm, with a lattice microstrain of about 0.65–0.87%. After heating, we noted an increase in crystallite size up to 95 nm.

The thermal analysis of the mechanically alloyed sample determined the Curie temperature at around 675 K, and its crystallization occurs by several exothermic reactions, indicating the improvement of the microstructure and reordering process. Compared with the ball-milled sample, the annealed sample with two heating cycles at 1373 K for 2 h and then at 1073 K for 24 h had a 12 K decrease in T_C heating. This decrease was related to extrinsic and intrinsic contributions in the material. For extended annealing temperatures, we noticed a large exothermic transformation, indicating a good crystallized system with large grains devoid of structural defects such as dislocations.

An examination of the magnetic properties revealed that the annealed alloy had superparamagnetic capabilities and that the mechanically alloyed powder displayed an extraordinarily soft ferromagnetic state for 15 h.

A new line of investigation into the susceptibility χ vs. T and that of χT vs. T in the vanishing field limit will be made possible by the remarkable magnetic transition between

a ferromagnetic regime below T_c and superparamagnetic behavior following the Curie law above T_c expected during this study, and its dependence on changes in the stacking type structure. This will permit a better interpretation of the hysteresis cycles.

Author Contributions: Conceptualization, M.K. and J.-J.S.; formal analysis, N.K. and M.M.A.; investigation, N.K. and A.W.; data curation, N.K. and A.W.; writing—original draft preparation, N.K.; writing—review and editing, M.K. and A.M.; supervision, J.-J.S. All authors have read and agreed to the published version of the manuscript.

Funding: This research was funded by the University of Girona, grant number PONT2020-01.

Data Availability Statement: Data available upon request to the authors.

Acknowledgments: We acknowledge the support of the University of Girona Technical Services.

Conflicts of Interest: The authors declare no conflicts of interest.

References

1. Brück, E. Developments in magnetocaloric refrigeration. *J. Phys. D Appl. Phys.* **2005**, *38*, R381. [\[CrossRef\]](#)
2. Brück, E.; Tegus, O.; Thanh, D.T.C.; Buschow, K.H.J. Magnetocaloric refrigeration near room temperature (invited). *J. Magn. Magn. Mater.* **2007**, *310*, 2793–2799. [\[CrossRef\]](#)
3. Tegus, O.; Bruck, E.; Buschow, K.H.J.; De Boer, F.R. Transition-metal-based magnetic refrigerants for room-temperature applications. *Nat. Lond.* **2002**, *415*, 150. [\[CrossRef\]](#)
4. Gschneidner, K.A.; Pecharsky, V.K.; Tsokol, A.O. Recent developments in magnetocaloric materials. *Rep. Prog. Phys.* **2005**, *68*, 1479. [\[CrossRef\]](#)
5. Brück, E.; Tegus, O.; Thanh, D.T.C.; Trung, N.T.; Buschow, K.H.J. A review on Mn-based materials for magnetic refrigeration: Structure and properties. *Int. J. Refrig.* **2008**, *31*, 763. [\[CrossRef\]](#)
6. Gutfleisch, O.; Willard, M.A.; Brück, E.; Chen, C.H.; Sankar, S.G.; Liu, J.P. Magnetic Materials and Devices for the 21st Century: Stronger, Lighter, and More Energy Efficient. *Adv. Mater.* **2011**, *23*, 821. [\[CrossRef\]](#)
7. Trung, N.T.; Gortemulder, Z.Q.; Ou, T.J.; Tegus, O.; Buschow, K.H.J.; Brück, E. Tunable thermal hysteresis in MnFe(P,Ge) compounds. *Appl. Phys. Lett.* **2009**, *94*, 102513. [\[CrossRef\]](#)
8. Gottschall, T.; Skokov, K.P.; Fries, M.; Taubel, A.; Radulov, I.; Scheibel, F.; Benke, D.; Riegg, S.; Gutfleisch, O. Making a cool choice: The materials library of magnetic refrigeration. *Adv. Energy Mater.* **2019**, *9*, 1901322. [\[CrossRef\]](#)
9. Guillou, F.; Porcari, G.; Yibole, H.; van Dijk, N.; Brück, E. Taming the first-order transition in giant magnetocaloric materials. *Adv. Mater.* **2014**, *26*, 2671–2675. [\[CrossRef\]](#)
10. Miao, X.F.; Caron, L.; Roy, P.; Dung, N.H.; Zhang, L.; Kockelmann, W.A.; De Groot, R.A.; van Dijk, N.H.; Brück, E. Tuning the phase transition in transition-metal-based magnetocaloric compounds. *Phys. Rev. B* **2014**, *89*, 174429. [\[CrossRef\]](#)
11. Caron, L.; Trung, N.T.; Brück, E. Pressure-tuned magnetocaloric effect in Mn_{0.93}Cr_{0.07}CoGe. *Phys. Rev. B* **2011**, *84*, 020414. [\[CrossRef\]](#)
12. Guillou, F.; Wilhelm, F.; Tegus, O.; Rogalev, A. Microscopic mechanism of the giant magnetocaloric effect in MnCoGe alloys probed by x-ray magnetic circular dichroism. *Appl. Phys. Lett.* **2016**, *108*, 122405. [\[CrossRef\]](#)
13. Liu, J.; Gong, Y.Y.; Xu, G.Z.; Peng, G.; Shah, I.A.; UlHassan, N.; Xu, F. Realization of magnetostructural coupling by modifying structural transitions in MnNiSiCoNiGe system with a wide Curie-temperature window. *Sci. Rep.* **2016**, *6*, 23386. [\[CrossRef\]](#)
14. Liu, E.K.; Wang, W.H.; Feng, L.; Zhu, W.; Li, G.J.; Chen, J.L.; Zhang, H.W.; Wu, G.H.; Jiang, C.B.; Xu, H.B.; et al. Stable magnetostructural coupling with tunable magneto-responsive effects in hexagonal ferromagnets. *Nat. Commun.* **2012**, *3*, 873. [\[CrossRef\]](#)
15. Johnson, V.; Fredbrick, C.G. Magnetic and crystallographic properties of ternary manganese silicides with ordered Co₂P structure. *Phys. Status Solidi A* **1973**, *20*, 331. [\[CrossRef\]](#)
16. Dung, N. Moment Formation and Giant Magnetocaloric Effects in Hexagonal Mn-Fe-P-Si Compounds. Ph.D. Thesis, Delft University of Technology, Delft, The Netherlands, 2012.
17. Wada, H.; Takahara, T.; Katagiri, K.; Ohnishi, T.; Soejima, K.; Yamashita, K. Recent progress of magnetocaloric effect and magnetic refrigerant materials of Mn compounds (invited). *J. Appl. Phys.* **2015**, *117*, 172606. [\[CrossRef\]](#)
18. Guillou, F.; Yibole, H.; van Dijk, N.H.; Brück, E. Effect of boron substitution on the ferromagnetic transition of MnFe_{0.95}P_{2/3}Si_{1/3}. *J. Alloys Compd.* **2015**, *632*, 717–722. [\[CrossRef\]](#)
19. Guillou, F.; Yibole, H.; van Dijk, N.; Zhang, L.; Hardy, V.; Brück, E. About the mechanical stability of MnFe(P,Si,B) giant-magnetocaloric materials. *J. Alloys Compd.* **2014**, *617*, 569–574. [\[CrossRef\]](#)
20. Miao, X.F.; Hu, S.Y.; Xu, F.; Brück, E. Overview of magnetoelastic coupling in (Mn,Fe)₂(P, Si)-type magnetocaloric materials. *Rare Met.* **2018**, *37*, 723–733. [\[CrossRef\]](#)
21. Fujii, S.; Asano, S.; Ishida, S. Electronic and magnetic properties of X₂Mn_{1-x}V_xSi (X = Fe, Co). *J. Phys. Soc. Jpn.* **1994**, *63*, 1881–1888. [\[CrossRef\]](#)
22. Rundqvist, S. X-ray investigations of Mn₃P, Mn₂P, and Ni₂P. *Acta Chem. Scand.* **1962**, *16*, 992–998. [\[CrossRef\]](#)

23. Zhanga, F.; Taake, C.; Huang, B.; You, X.; Ojiyed, H.; Shen, Q.; Dugulan, I.; Caronb, L.; Dijka, N.V.; Brück, E. Magnetocaloric effect in the $(\text{Mn,Fe})_2(\text{P,Si})$ system: From bulk to nano. *Acta Mater.* **2022**, *224*, 117532. [[CrossRef](#)]
24. Miao, X.F.; Caron, L.; Cedervall, J.; Gubbens, P.C.M.; Dalmas de Réotier, P.; Yaouanc, A.; Qian, F.; Wildes, A.R.; Luetkens, H.; Amato, A.; et al. Short-range magnetic correlations and spin dynamics in the paramagnetic regime of $(\text{Mn,Fe})_2(\text{P, Si})$. *Phys. Rev. B* **2016**, *94*, 014426. [[CrossRef](#)]
25. Daly, R.; Khitouni, M.; Kolsi, A.W.; Njah, N. The studies of crystallite size and microstrains in aluminum powder prepared by mechanical milling. *Phys. Stat. Solidi C* **2006**, *3*, 3325–3331. [[CrossRef](#)]
26. Khitouni, M.; Kolsi, A.W.; Njah, N. The effects of boron additions on the disordering and crystallite refinement of Ni_3Al powders during mechanical milling. *Ann. De Chim. Sci. Matériaux* **2003**, *28*, 17–29. [[CrossRef](#)]
27. Berak, J.; Heumann, T. Über das System Mangan-Phosphor. *Int. J. Mater. Res.* **1950**, *41*, 19–23. [[CrossRef](#)]
28. Lai, J.W.; Zheng, Z.G.; Huang, B.W.; Yu, H.Y.; Qiu, Z.G.; Mao, Y.L.; Zhang, S.; Xiao, F.M.; Zeng, D.C.; Goubitz, K.; et al. Microstructure formation and magnetocaloric effect of the Fe_2P -type phase in $(\text{Mn,Fe})_2(\text{P, Si, B})$ alloys. *J. Alloys Compd.* **2018**, *735*, 2567–2573. [[CrossRef](#)]
29. Fowley, C.; Rode, K.; Lau, Y.C.; Thiyagarajah, N.; Betto, D.; Borisov, K.; Atcheson, G.; Kampert, E.; Wang, Z.; Yuan, Y.; et al. Magnetocrystalline anisotropy and exchange probed by high-field anomalous Hall effect in fully compensated half-metallic Mn_2RuxGa thin films. *Phys. Rev. B* **2018**, *98*, 220406. [[CrossRef](#)]
30. Betto, D.; Lau, Y.C.; Borisov, K.; Kummer, K.; Brookes, N.B.; Stamenov, P.; Coey, J.M.D.; Rode, K. Structure, site-specific magnetism, and magnetotransport properties of epitaxial D022-structure Mn_2FexGa thin films. *Phys. Rev. B* **2017**, *96*, 024408. [[CrossRef](#)]
31. Levin, E.E.; Bocarsly, J.D.; Grebenkemper, J.H.; Issa, R.; Wilson, S.D.; Pollock, T.M.; Seshadri, R. Structural coupling and magnetic tuning in $\text{Mn}_{2-x}\text{Co}_x\text{P}$ magnetocalorics for thermomagnetic power generation. *APL Mater.* **2020**, *8*, 041106. [[CrossRef](#)]
32. Singh, A.K.; Singh, V.; Bhattacharjee, S.; Lee, S.-C.; Singh, S.; Pandey, D. Effect of heat treatment on the phase purity of Fe_2P powder. *AIP Conf. Proc.* **2020**, *2265*, 030021. [[CrossRef](#)]
33. Gutfleisch, O.; Gottschall, T.; Fries, M.; Benke, D.; Radulov, I.; Skokov, K.P.; Wende, H.; Gruner, M.; Acet, M.; Entel, P.; et al. Mastering hysteresis in magnetocaloric materials. Philosophical Transactions of the Royal Society A: Mathematical. *Phys. Eng. Sci.* **2016**, *374*, 20150308. [[CrossRef](#)]
34. Schaffer, G.B.; McCormick, P.G. Mechanical alloying. *Mater. Forum* **1992**, *16*, 91–97.
35. Coey, J.M.D. Magnetic materials. *J. Alloys Compd.* **2001**, *326*, 2–6. [[CrossRef](#)]
36. Degauque, J. Magnétisme et matériaux magnétiques: Introduction. *J. Phys. IV* **1992**, *2*, C3-1–C3-13. [[CrossRef](#)]
37. Nowroozi, M.A.; Shokrollahi, H. The effects of milling time and heat treatment on the micro-structural and magnetic behavior of $\text{Fe}_{42}\text{Ni}_{28}\text{Zr}_8\text{Ta}_2\text{B}_{10}\text{C}_{10}$ synthesized by mechanical alloying. *J. Magn. Magn. Mater.* **2013**, *335*, 53–58. [[CrossRef](#)]
38. Zhang, K.B.; Fu, Z.Y.; Zhang, J.Y.; Shi, J.; Wang, W.M.; Wanga, H.; Wang, Y.C.; Zhang, Q.J. Annealing on the structure and properties evolution of the CoCrFeNiCuAl high-entropy alloy. *J. Alloys Compd.* **2010**, *502*, 295–299. [[CrossRef](#)]
39. Ji, W.; Wang, W.; Wang, H.; Zhang, J.; Wang, Y.; Zhang, F.; Fu, Z. Alloying behavior and novel properties of CoCrFeNiMn high-entropy alloy fabricated by mechanical alloying and spark plasma sintering. *Intermetallics* **2015**, *56*, 24–27. [[CrossRef](#)]
40. Feng, J.J.; Gao, S.; Han, K.; Miao, Y.D.; Qi, J.Q.; Wei, F.X.; Ren, Y.J.; Zhan, Z.Z.; Sui, Y.W.; Sun, Z.; et al. Effects of minor B addition on microstructure and properties of $\text{Al}_{19}\text{Co}_{20}\text{Fe}_{20}\text{Ni}_{41}$ eutectic high-entropy alloy. *Trans. Nonferrous Met. Soc. China* **2021**, *31*, 1049–1058. [[CrossRef](#)]
41. Wang, X.F.; Zhang, Y.; Qiao, Y.; Chen, G.L. Novel microstructure and properties of multicomponent CoCrCuFeNiTi_x alloys. *Intermetallics* **2007**, *15*, 357–362. [[CrossRef](#)]
42. Zhang, Y.; Zuo, T.T.; Tang, Z.; Gao, M.C.; Dahmen, K.A.; Liaw, P.K.; Lu, Z.P. Microstructures and properties of high-entropy alloys. *Prog. Mater. Sci.* **2014**, *61*, 1–93. [[CrossRef](#)]
43. Shinde, S.R.; Ogale, S.B.; Higgins, J.S.; Zheng, H.; Millis, A.J.; Kulkarni, V.N.; Ramesh, R.; Greene, R.L.; Venkatesan, T. Co-occurrence of superparamagnetism and anomalous Hall effect in highly reduced cobalt-doped rutile $\text{TiO}_{2-\delta}$ films. *Phys. Rev. Lett.* **2004**, *92*, 166601. [[CrossRef](#)]
44. Fujii, H.; Hokabe, T.; Kamigaichi, T.; Okamoto, T. Magnetic Properties of Fe_2P Single Crystal. *J. Phys. Soc. Jpn.* **1977**, *43*, 41. [[CrossRef](#)]
45. Fan, X.; Tan, F.; Zhang, G.; Zhang, F. A novel strategy to fabricate $\gamma\text{-Fe}_2\text{O}_3$ -MWCNTs hybrids with selectively ferromagnetic or superparamagnetic properties. *Mater. Sci. Eng. A* **2007**, *454*, 37–42. [[CrossRef](#)]
46. Liu, X.; Liu, J.P.; Zhang, Q.; Altounian, Z. Fe magnetic moment formation and exchange interaction in Fe_2P : A first-principles study. *Phys. Lett. A* **2013**, *377*, 731. [[CrossRef](#)]
47. Bortolotti, M.; Lutterotti, L.; Pepponi, G. Combining XRD and XRF analysis in one Rietveld-like fitting. *Powder Diffr.* **2017**, *32*, S225–S230. [[CrossRef](#)]
48. Rietveld, H.M. A profile refinement method for nuclear and magnetic structures. *J. Appl. Crystallogr.* **1969**, *2*, 65–71. [[CrossRef](#)]
49. Warren, B.E.; Averbach, B.L. The Effect of Cold-Work Distortion on X-ray Patterns. *J. Appl. Phys.* **1950**, *21*, 595–599. [[CrossRef](#)]
50. Williamson, G.K.; Hall, W.H. X-ray line broadening from filed aluminium and wolfram. *Acta Metall.* **1953**, *1*, 22–31. [[CrossRef](#)]

Disclaimer/Publisher’s Note: The statements, opinions and data contained in all publications are solely those of the individual author(s) and contributor(s) and not of MDPI and/or the editor(s). MDPI and/or the editor(s) disclaim responsibility for any injury to people or property resulting from any ideas, methods, instructions or products referred to in the content.